

Article

Effect of Sintering Temperature on Structural, Dielectric, and Magnetic Properties of Multiferroic YFeO₃ Ceramics Fabricated by Spark Plasma Sintering

Meng Wang ^{1,†}, Ting Wang ^{1,†}, Shenhua Song ^{1,*}, Qing Ma ^{2,3,*} and Renchen Liu ^{2,3}

¹ Shenzhen Key Laboratory of Advanced Materials, Department of Materials Science and Engineering, Shenzhen Graduate School, Harbin Institute of Technology, Shenzhen 518055, China; wangmeng1985@hit.edu.cn (M.W.); twang-hawk@foxmail.com (T.W.)

² Research Institute of Tsinghua University in Shenzhen, Shenzhen 518055, China; renchen.liu@gmail.com

³ Tsinghua Innovation Center in Dongguan, Dongguan 523808, China

* Correspondence: shsong@hit.edu.cn (S.S.); wustmq@163.com (Q.M.); Tel.: +86-755-2603-3465 (S.S.)

† These authors contributed equally to this work.

Academic Editor: Beatriz Noheda

Received: 2 December 2016; Accepted: 23 February 2017; Published: 7 March 2017

Abstract: Based on precursor powders with a size of 200–300 nm prepared by the low-temperature solid reaction method, phase-pure YFeO₃ ceramics are fabricated using spark plasma sintering (SPS) at different temperatures. X-ray diffraction (XRD) and scanning electron microscopy (SEM) reveal that the high-purity YFeO₃ ceramics can be prepared using SPS, while the results from X-ray photoelectron spectroscopy (XPS) show that the concentration of oxygen vacancies resulting from transformation from Fe³⁺ to Fe²⁺ is low. The relative density of the 1000 °C-sintered sample is as high as 97.7%, which is much higher than those of the samples sintered at other temperatures. The present dielectric and magnetic properties are much better than those of the samples fabricated by conventional methods. These findings indicate that the YFeO₃ ceramics prepared by the low temperature solid reaction and SPS methods possess excellent dielectric and magnetic properties, making them suitable for potential applications involving magnetic storage.

Keywords: multiferroic materials; spark plasma sintering; low-temperature solid reaction; dielectric properties; magnetic properties

1. Introduction

In recent years, a novel material coupled with two or more magnetic, electric, and elastic orders, commonly referred to as multiferroic material, has become the focus of scientific and industrial interest because of its unusual properties, with potential applications in telecommunication and memory devices. For example, second generation multiferroic materials, such as RFeO₃ (R = Gd, Er, La, Yb, Lu, and Y), have attracted much research attention. Unlike the first generation multiferroic materials possessing high ferroelectricity and low ferromagnetism, the RFeO₃ groups not only combine ferroelectric and anti-ferromagnetic properties but also show favorable magnetoelectric coupling effects [1–4].

The purpose of this paper is to describe a method used to fabricate YFeO₃ ceramics by a low-temperature solid reaction method along with spark plasma sintering. YFeO₃ is not only widely studied but also possesses antiferromagnetic nature with a high Néel temperature ($T_N = 640$ K) and excellent dielectric property at room temperature. Although normal ferroelectricity is not possible in YFeO₃ due to its space group of symmetrical Pnma, it is still worthwhile to investigate its dielectric characteristics, magnetic ordering related to dielectric relaxations, and potential ferroelectricity [5–8].

However, fabrication methods restrain the preparation of high-quality YFeO₃. Most studies adopted the conventional solid state reaction method to fabricate YFeO₃ [9,10]. The main disadvantages

of this method are: (1) the preparation process includes complex procedures, such as preheat, sintering, and heat treatment; (2) high calcination temperature and long sintering time are needed; and (3) some secondary phases are usually introduced during the process. These impurities can have a severe impact on the magnetic properties of the material. For instance, remnant magnetization and coercive field of YFeO_3 ceramics prepared via the conventional solid-state method is as low as 0.81 emu/g and 1 kOe, respectively [10]. These levels limit the potential application of YFeO_3 ceramics.

Another precursor fabrication candidate is the sol-gel method. Wu et al. [11], Racu et al. [12] and Shang et al. [13] successfully prepared YFeO_3 powders by the sol-gel method and Zhang et al. [14] developed a one-step synthesis of YFeO_3 nanocrystals via a sol-gel auto-combustion method. The main drawbacks of this method are (1) the size of the particles increases to a submicron scale and (2) when the powders are used to prepare ceramics, many pores are introduced, resulting in a material with relatively low density [9,10,15,16]. So a simple and high efficiency method should be developed for YFeO_3 powder preparation.

In view of this situation, a method for precursor fabrication, namely the low-temperature solid reaction method, has the advantage of easy phase control, pure phase production, low cost, and ultrafine particle size. It only needs grinding in an agate mortar to fabricate precursors, so the procedure is greatly simplified. This method was successfully adopted to obtain YMnO_3 and ZnFe_2O_4 precursors [17]. Therefore, this method may be used to synthesize fine YFeO_3 precursor powders.

Recently, spark plasma sintering (SPS) has been aggressively adopted as an advanced method for powder metallurgy fabrication. One notable feature of SPS is that it allows the use of a low sintering temperature (200–300 K lower than that of the conventional method) and a short sintering time (typically only 5 min), so that high-density structures can be obtained [18–21]. Ma et al. have developed dense $\text{Y}(\text{Mn,Fe})\text{O}_3$ and YMnO_3 nano-size ceramics [22,23]. Song et al. and Wang et al. obtained BiFeO_3 nano-ceramics using precursors prepared by ball milling and sol-gel methods, respectively [24,25]. However, it should be pointed out that even using the SPS method, the impure phase still exists and the grain size still needs to be precisely controlled.

Two important aspects of the study are emphasized. They include an SPS fabrication procedure with a low-temperature solid reaction precursor preparation method along with annealing in air to produce the YFeO_3 ceramic and the sintering temperatures for SPS processes. The microstructures of YFeO_3 precursor and ceramics were studied extensively. The dielectric characteristics of YFeO_3 ceramics were evaluated over broad temperature and frequency ranges. The relationship between the magnetic properties and microstructures of the fabricated YFeO_3 samples was also studied.

2. Experimental Procedures

In this study, YFeO_3 powders were synthesized via the low-temperature solid reaction method. The raw reagents include $\text{Fe}(\text{NO}_3)_3 \cdot 9\text{H}_2\text{O}$, $\text{Y}(\text{NO}_3)_3 \cdot 6\text{H}_2\text{O}$, and citric acid. Initially, $\text{Fe}(\text{NO}_3)_3 \cdot 9\text{H}_2\text{O}$, $\text{Y}(\text{NO}_3)_3 \cdot 6\text{H}_2\text{O}$ and citric acid under a mole ratio of 1:1:2 were weighed and ground in an agate mortar for half an hour, respectively. Then the respective powders were mixed and ground again in an agate mortar for half an hour. A light brown viscous substance was formed during the grinding process, implying that the complex was formed. The viscous substance was heated at 120 °C for 2 h to remove free water and then a powdery composite was harvested, serving as the precursor material. The powders were ground and subsequently calcined for 1 h in air at 800 °C to provide what shall be referred to as the pure phase YFeO_3 powders, serving as raw precursors for the subsequent SPS process. In the SPS process, the YFeO_3 powders were placed in a graphite die and heated at a rate of 100 °C/min from room temperature to 900, 950, 1000, and 1050 °C, respectively, followed by sintering for 5 min under an atmospheric pressure of 10^{-2} Pa. During the entire SPS process, a uniaxial pressure of 50 MPa was constantly maintained to the sample [26]. After completing the sintering process, pellet-shaped samples were formed. The samples were then polished to a size of 2 mm thick and 10 mm diameter, followed by annealing at 800 °C for 2 h in air in order to recover the oxygen stoichiometric ratio, release strain, and remove carbon contamination.

The crystal structures of the pellet samples were analyzed using X-ray Diffraction (XRD) (D/max-RB, Rigaku, Tokyo, Japan). The fracture surfaces of the samples were observed using scanning electron microscopy (S-4700, Hitachi, Tokyo, Japan). The densities of the pellets were measured via traditional Archimedes method with distilled water. X-ray photoelectron spectroscopy (XPS) measurements were carried out on an ESCALAB 250Xi system (ESCALAB 250Xi, Perkin Elmer, Waltham, MA, USA) with Mg $K\alpha$ radiation. The XPS curves were fitted with XPS-Peakfit software through Gauss-Lorentz line. All the samples were then polished to 1 mm thick, sprayed with silver paint, and cured for 1 h at 120 °C. This procedure was required in order to prepare the test samples for dielectric measurements. Magnetic properties of the samples were obtained using a physical property measurement system (DynaCool-9T, Quantum Design, Leatherhead, Surrey, UK) at room temperature.

3. Results and Discussion

Figure 1a reveals the XRD pattern of the precursor powders prepared via the low-temperature solid reaction method. Clearly, the diffraction peaks are well-fitted to the $YFeO_3$ phase possessing an orthorhombic perovskite structure with space group of $Pnma$. No visible impure phases (such as Y_2O_3 , Fe_2O_3 , and $Y_3Fe_5O_{12}$) can be detected in the powders within the limits of the XRD machine capability. Consequently, high-purity powders are successfully obtained. Figure 1b shows the SEM micrograph of the $YFeO_3$ precursor powders. The particles appear to be homogeneous in the size range of ~200–300 nm.

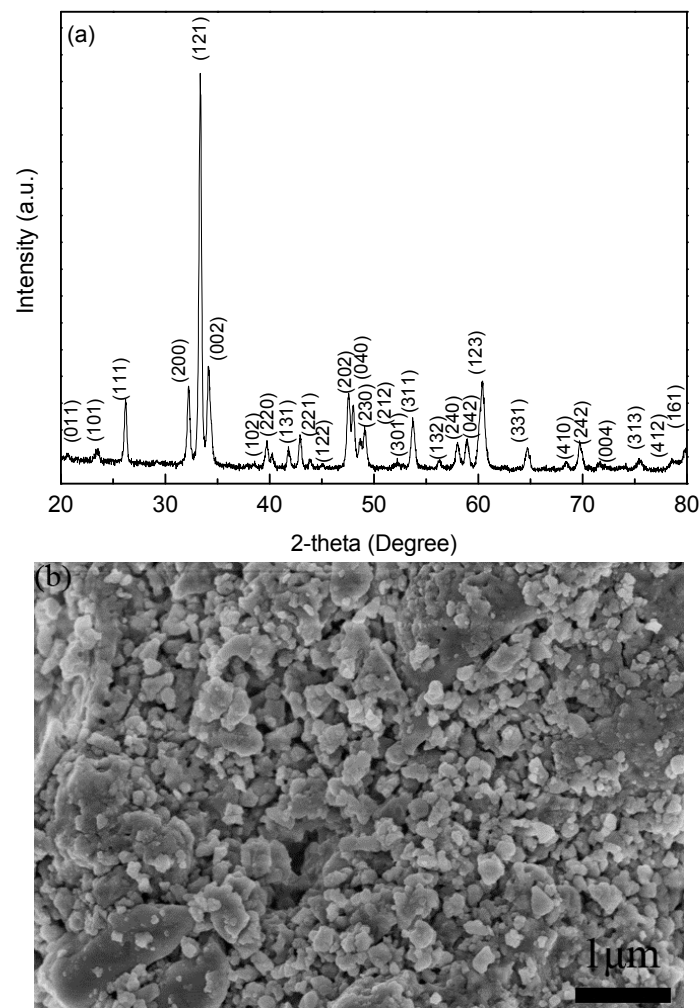


Figure 1. (a) XRD pattern and (b) SEM micrograph for $YFeO_3$ powders.

XRD patterns of the SPS-prepared samples sintered at different temperatures are shown in Figure 2. The unique high-purity phase pattern is presented in the 1000 °C-sintered sample. As for the 900 °C and 950 °C-sintered samples, the secondary phase Y_2O_3 (heart shaped symbol) can be detected. The transformation of $Y_2O_3 + Fe_2O_3 \leftrightarrow 2YFeO_3$ is common in the range of 900–1000 °C. The pattern for the 1050 °C-sintered sample suggests the presence of $Y_3Fe_5O_{12}$. The transformation from the orthorhombic perovskite $YFeO_3$ to $Y_3Fe_5O_{12}$ and Y_2O_3 ($5YFeO_3 \leftrightarrow Y_3Fe_5O_{12} + Y_2O_3$) is normal around 1100 °C, and it is probably because an extra energy is supplied by SPS. Accordingly, this transformation can occur in the 1050 °C-sintered sample. This behavior is in accordance with the finding reported in [27]. In summary, the unique $YFeO_3$ phase without impurities can only be acquired for the 1000 °C-sintered sample, which is 300–400 °C lower compared to conventional methods.

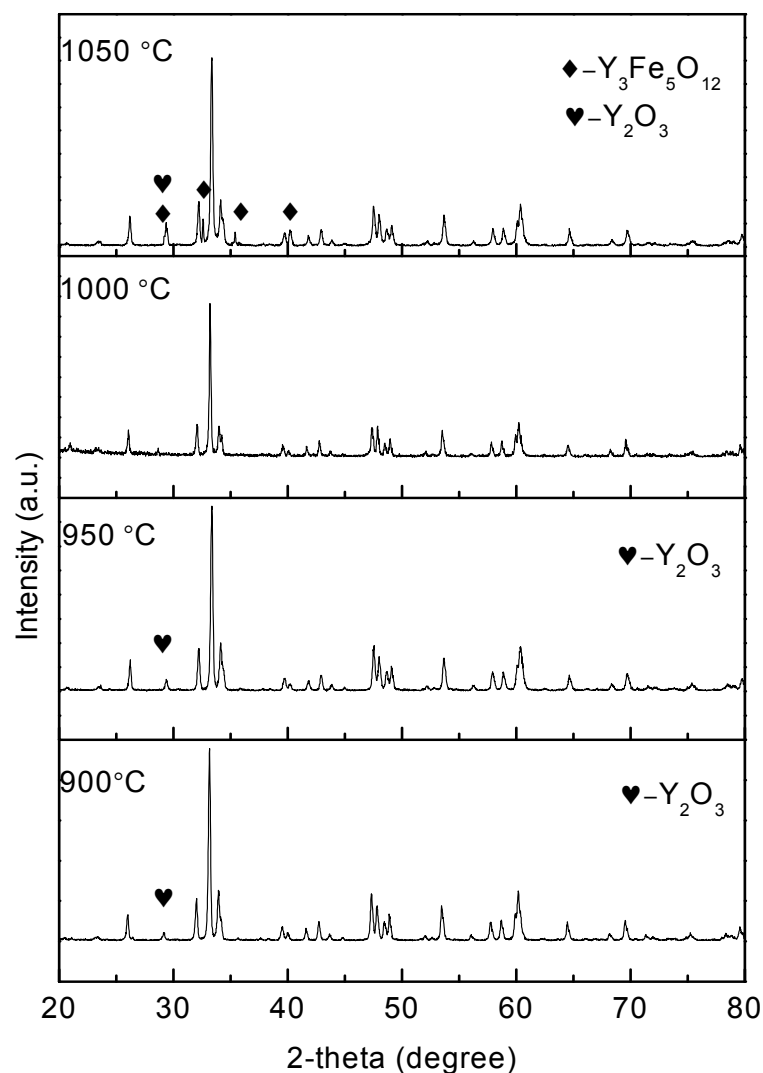


Figure 2. XRD patterns for $YFeO_3$ samples sintered at different temperatures (900, 950, 1000, and 1050 °C).

SEM micrographs of the fracture surfaces of the samples sintered at four different temperatures are shown in Figure 3. Normally, the fracture surface, rather than thermally etched polished cross-sections of samples, is a good way to present the real morphology and defects in ceramics. For the cases of sintering at 900 °C and 950 °C, the samples show large cracks and pores, proving that these samples were not successfully sintered. Meanwhile, the 1000 °C- and 1050 °C-sintered samples exhibit a high-density $YFeO_3$ structure with smooth facets. After the SPS sintering and annealing process, the

grain size of the sintered ceramics increases to $\sim 1\text{--}2\ \mu\text{m}$ for the $1000\ ^\circ\text{C}$ -sintered sample and $\sim 5\text{--}8\ \mu\text{m}$ for the $1050\ ^\circ\text{C}$ -sintered sample. The increase in grain size is due to the higher sintering temperature ($1000\text{--}1050\ ^\circ\text{C}$) during the SPS process compared with the temperatures used in the calcining process of YFeO_3 powders ($800\ ^\circ\text{C}$). As for the $1050\ ^\circ\text{C}$ -sintered sample, the lower densities of impurities $\text{Y}_3\text{Fe}_5\text{O}_{12}$ and Y_2O_3 can lead to a volume expansion at the elevated sintering temperature. These effects can result in a surface with more pores and defects [28].

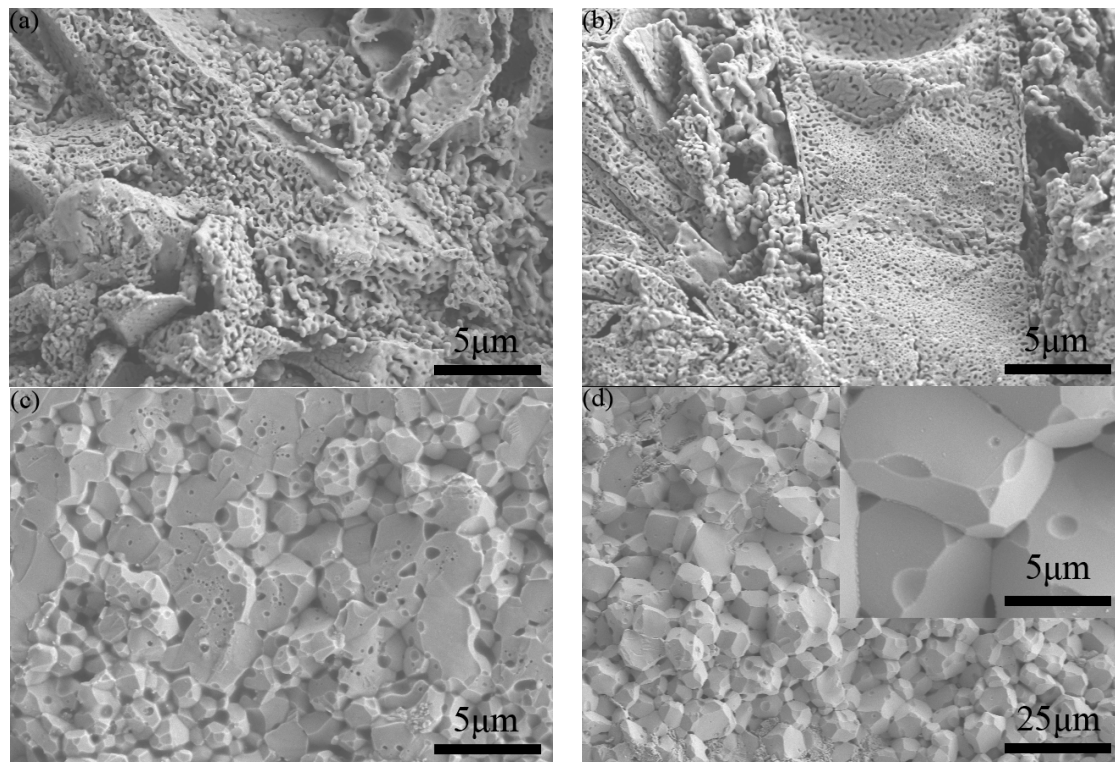


Figure 3. SEM micrographs of fracture surfaces of the YFeO_3 ceramics sintered at different temperatures: (a) $900\ ^\circ\text{C}$; (b) $950\ ^\circ\text{C}$; (c) $1000\ ^\circ\text{C}$; (d) $1050\ ^\circ\text{C}$.

The densities of the YFeO_3 pellet samples are shown in Figure 4. Before annealing, the density of the $1000\ ^\circ\text{C}$ -sintered sample reaches its highest value of $5.484\ \text{g}/\text{cm}^3$. This value is equivalent to a relative density of 96.5% (theoretical density = $5.68\ \text{g}/\text{cm}^3$). For the $900\ ^\circ\text{C}$ and $950\ ^\circ\text{C}$ -sintered ceramics, the densities of $4.023\ \text{g}/\text{cm}^3$ and $4.625\ \text{g}/\text{cm}^3$ are obtained, respectively. These are only 70.8% and 81.4% of the theoretical density, suggesting that the sintering process is not fully completed. For the $1050\ ^\circ\text{C}$ -sintered sample, the density is slightly lower than that of the $1000\ ^\circ\text{C}$ -sintered sample because the secondary phase $\text{Y}_3\text{Fe}_5\text{O}_{12}$ and Y_2O_3 are introduced and more defects exist [9,29]. After annealing, all the samples exhibit slightly higher densities as compared to those before annealing, probably because the deficiency of oxygen is compensated and the carbon contamination is eliminated during the annealing treatment. This outcome suggests that, under a simultaneous use of constant uniaxial pressure and high-density heat of plasma, YFeO_3 ceramics with high quality and density can be successfully prepared. Therefore, it is affirmed that the highly pure and dense YFeO_3 ceramics with fine-grained structures can be fabricated using precursor powders by means of SPS at $1000\ ^\circ\text{C}$ plus annealing at $800\ ^\circ\text{C}$ for 2 h in air.

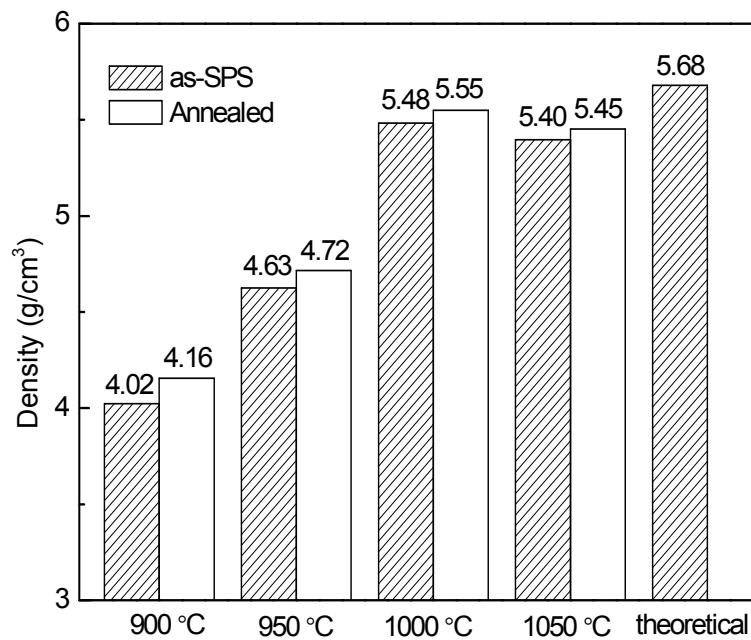


Figure 4. The densities of the samples after SPS and annealing.

Because the 900 °C- and 950 °C-sintered samples are not fully sintered, the 1000 °C- and 1050 °C-sintered samples will be only analyzed further. Since the ionic valence has an important effect on the dielectric and magnetic properties of materials, XPS spectra are determined on the YFeO_3 ceramics. Figure 5 depicts the Y 3d, Fe 2p, and O 1s XPS patterns of the 1000 °C- and 1050 °C-sintered YFeO_3 samples. Binding energy (BE) values are 157.2 eV and 159.0 eV for Y 3d_{3/2} and Y 3d_{5/2}, respectively, and $\Delta\text{Y 3d} = 1.8$ eV is in good agreement with the published results [30]. The Fe 2p_{3/2} peak, using Gauss-Lorentz fitting, is divided into two parts representing the coexistence of Fe³⁺ and a low percentage of Fe²⁺. The binding energies for Fe²⁺ 2p_{3/2} and Fe³⁺ 2p_{3/2} are 709.20 and 710.70 eV, respectively. These values not only agree well with the values presented in the published reports but validate the coexistence of Fe²⁺ and Fe³⁺ [12]. Evaluation of the peak spectra regions shows that the peak for Fe²⁺ ions is less than 10% of the entire Fe component. The peak for Fe²⁺ ions in the 1000 °C-sintered sample is 6.2% of the entire peak, while that in the 1050 °C-sintered sample reaches 8.9%. The reason for the emerging Fe²⁺ ions in the YFeO_3 sample is attributed to the presence of oxygen vacancies, which is unavoidable in RFeO_3 ceramic materials. However, the concentration of these ions is reasonably low. For the O 1s XPS pattern, two peaks are shown, namely one for lattice oxygen (O²⁻) at 528 eV and the other for surface absorbed oxygen (O⁻) at 532 eV [31]. The pattern shows that the height of the lattice oxygen (O²⁻) peak is lower than that of the surface absorbed oxygen (O⁻) peak. Also, both peak height and area of the lattice oxygen peak of the 1050 °C-sintered sample are much lower than those of the 1000 °C-sintered sample. This is likely due to the formation of oxygen vacancies. The formation of an oxygen vacancy can lead to the loss of an electron in the oxygen ion, resulting in a transfer from O²⁻ to O⁻ [32]. Therefore, it can be concluded that the concentration of oxygen vacancies in the 1000 °C-sintered sample is lower than that in the 1050 °C-sintered sample. This phenomenon can affect the dielectric and magnetic properties of materials. Also, the above analysis shows that it is possible to fabricate high-purity YFeO_3 at 1000 °C.

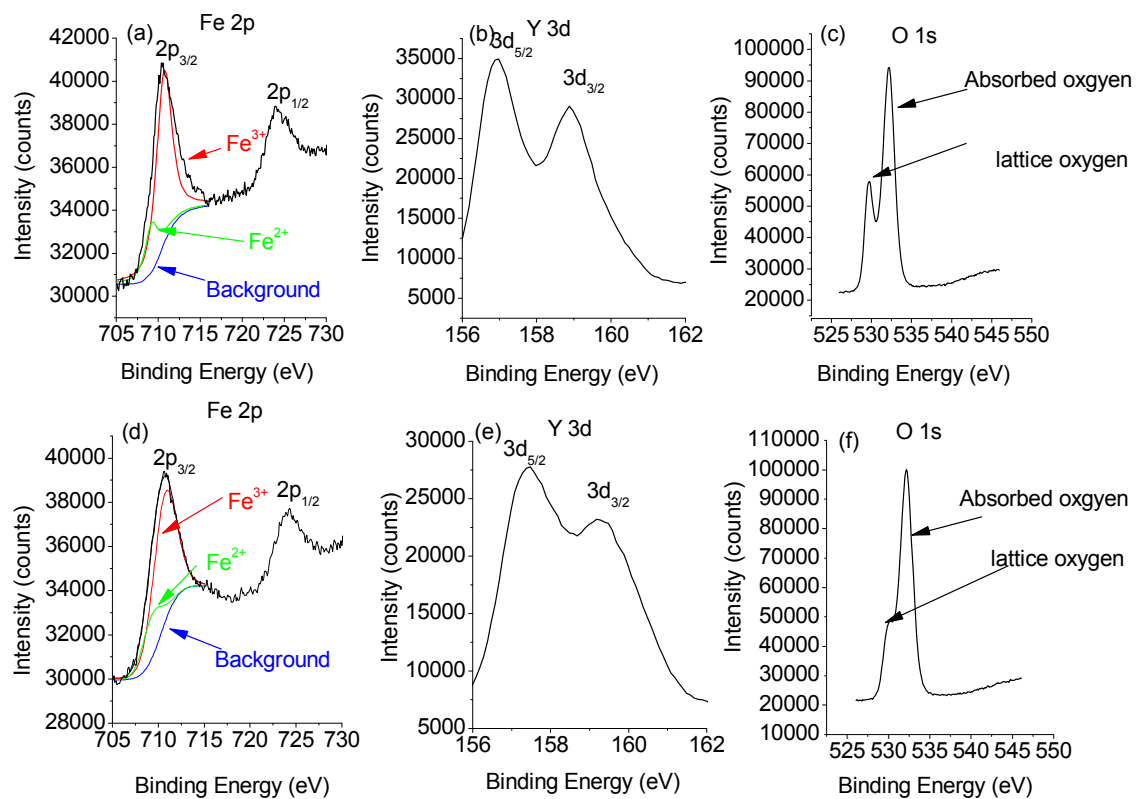


Figure 5. XPS spectra of the YFeO₃ ceramics: (a) Y 3d; (b) Fe 2p; and (c) O 1s for 1000 °C-sintered sample; (d) Y 3d; (e) Fe 2p; and (f) O 1s for 1050 °C-sintered sample.

Figure 6 shows the frequency dependences of dielectric loss at different temperatures for the samples sintered at 1000 °C and 1050 °C. Both diagrams (Figure 6a,b) show large values of dielectric loss in low frequency, which is due to the different conductivity between grain and grain boundary. With increasing frequency, the dielectric loss exhibits a gradual decrease for the 1000 °C-sintered sample, while for the 1050 °C-sintered sample, a peak is present from 10^5 to 10^6 Hz, showing the dielectric relaxation. As is commonly known, each polarization mechanism is characterized by a relaxation frequency corresponding to the maximal phase shift between the polarization and the applied electric field; thus a peak of dielectric loss occurs. The peak in Figure 6b is ascribed to space charge polarization. Usually, the space charge polarization is related to oxygen vacancies, as evidenced by XPS analysis in Figure 5. Because few oxygen vacancies emerged in the 1000 °C-sintered sample, no peak of dielectric loss can be seen. The dielectric constants as a function of frequency at room (25 °C) and elevated temperatures (160 °C and 200 °C) for the 1000 °C- and 1050 °C-sintered samples are shown in Figure 7. Both samples have a high value in the lower frequency range and drop drastically with increasing frequency above a turning point. The high values are associated to the high conductivity, the Maxwell-Wagner relaxation, which is often observed in heterogeneous systems with different conductivities. As the frequency increases, these factors are significantly damped out so that the space charges fail to comply with changes in the frequency of electrical field and result in a reduction in dielectric constant [33,34]. The dielectric constant shows a sharp decrease with increasing frequency in the low frequency range and a plateau in the high frequency region. Note that the plateau moves to higher frequencies with increasing temperature, which is an effect due to the Debye type thermally activated mechanism [22]. As shown in Figure 7, there is one plateau for the 1000 °C-sintered sample, but there are two for the 1050 °C-sintered sample, the first one of which is just corresponding to the relaxation peak shown in Figure 6b. This could be because the 1050 °C-sintered sample possesses more defects, such as pores and oxygen vacancies, as the space charges are related

to the defects, thereby resulting in a different polarization phenomenon. In addition, the dielectric constant is apparently higher for the 1000 °C-sintered sample, which is due to the lower oxygen vacancies, smaller grain size, and higher density of the sample (see Figures 3–5, respectively).

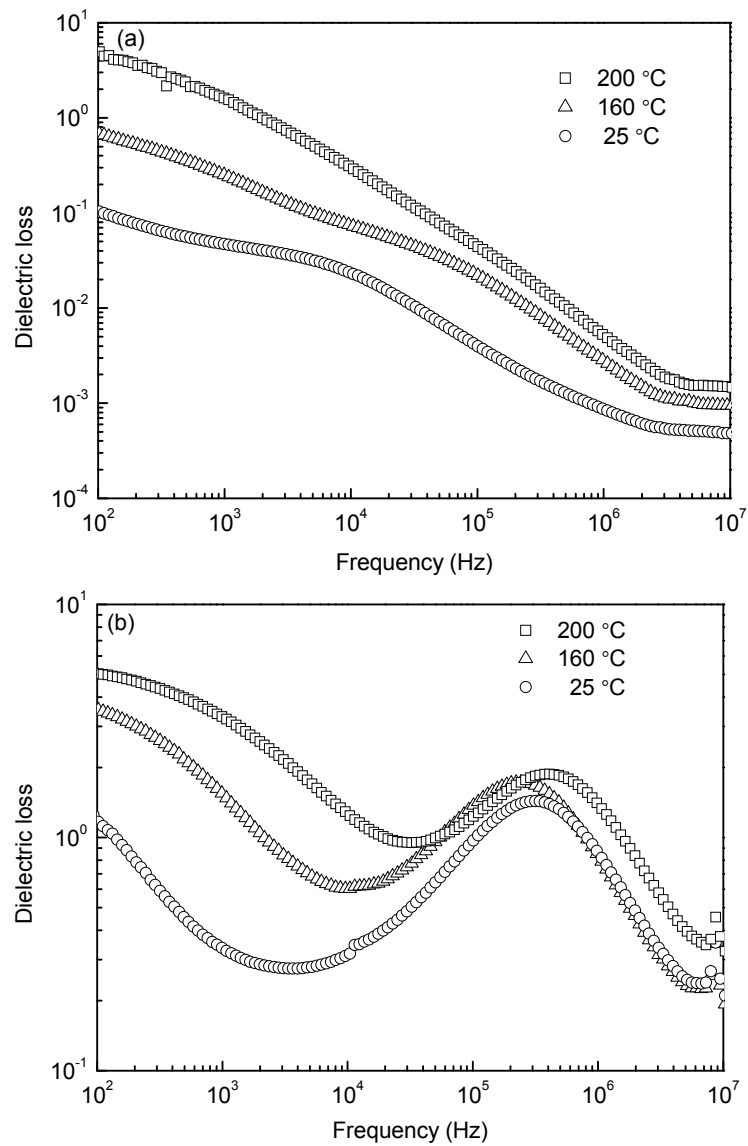


Figure 6. Frequency dependences of dielectric loss at different temperatures for the samples sintered at (a) 1000 °C and (b) 1050 °C.

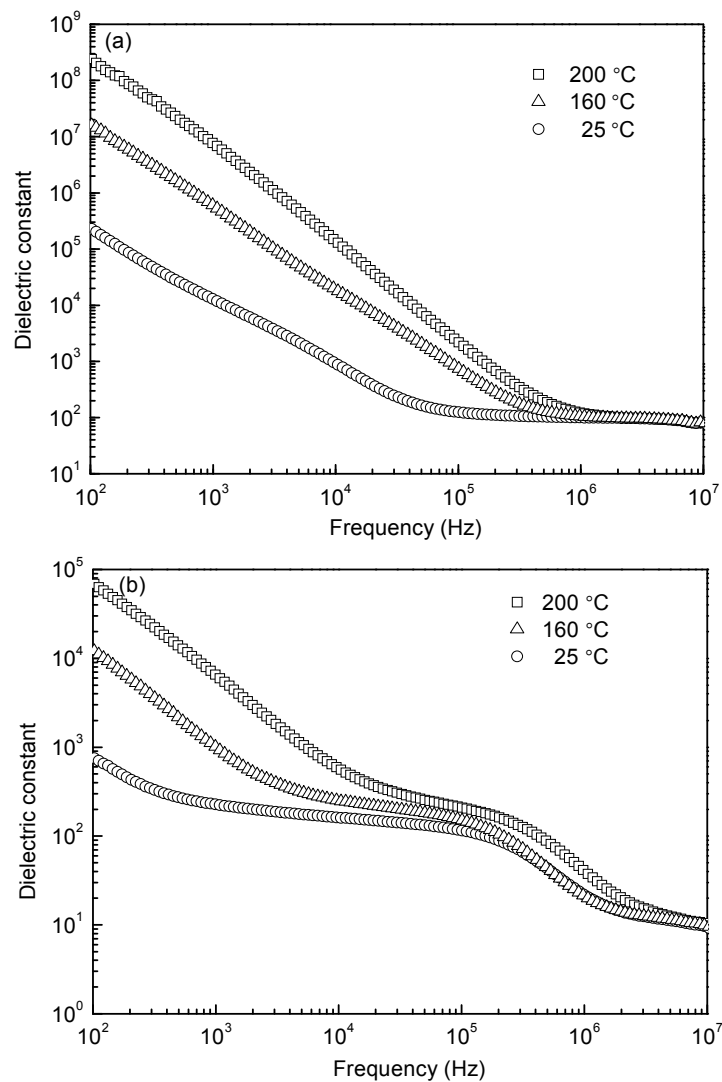


Figure 7. Frequency dependences of dielectric constant at different temperatures for the samples sintered at (a) 1000 °C and (b) 1050 °C

Figure 8 shows the temperature dependences of dielectric constant at the frequencies of 1 kHz, 10, 100, and 1 MHz for the 1000 °C- and 1050 °C-sintered samples. At a given temperature, the value of dielectric constant decreases with increasing frequency. In addition, the dielectric constant remains almost constant until 100 °C, and then starts to increase with further increasing temperature. An obvious dielectric relaxation effect can be observed in the range of 100–300 °C. Also note that this effect is delayed to higher temperatures as the frequency increases. The dielectric constant increases with increasing temperature and it is attributed to the conductivity enhancement. The overall dielectric constant values of the 1000 °C-sintered sample are much higher than those of the 1050 °C-sintered sample at 1 MHz (as higher frequencies can reflect the intrinsic dielectric constant of YFeO_3). For example, the dielectric constant of the 1000 °C-sintered sample at 1 MHz and 25 °C is 100, while that of the 1050 °C-sintered sample is about 20. The former is nearly five times higher than the latter, which can be ascribed to high resistance, lower oxygen vacancies, smaller grain size, and phase purities. An anomaly in dielectric constant for the 1050 °C-sintered sample, such as a sudden decrease, is also caused by the movement and concentration of point defects. This phenomenon does not exist in the 1000 °C-sintered sample probably because of the higher density and fewer pores of the sample, in addition to the constraint of grain boundaries on the mobility of these defects [35].

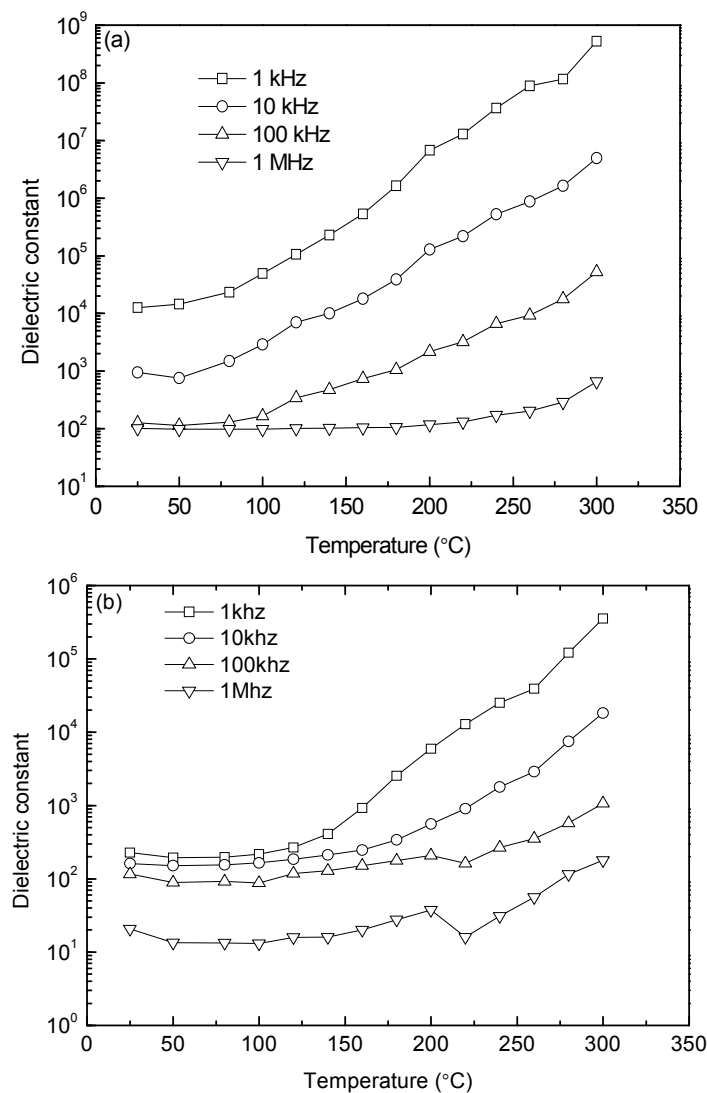


Figure 8. Temperature dependences of dielectric constant under frequencies of 1, 10, 100, and 1000 kHz for the samples sintered at (a) 1000 °C and (b) 1050 °C.

Room-temperature magnetic hysteresis loops of the YFeO_3 ceramic samples sintered at 1000 °C and 1050 °C are shown in Figure 9. It is well known that the ionic structure determines the anti-ferromagnetic property of YFeO_3 . Here a Fe^{3+} ion is surrounded by six O^{2-} ions, forming a FeO_6 octahedra, and each O^{2-} is the shared apex of two adjacent octahedras, serving as a super exchange interaction channel [36]. According to the Dzyaloshinski-Moriya anti symmetric exchange mechanism, each Fe^{3+} magnetic moment is located not totally parallel to the moments of all six nearest Fe^{3+} neighboring moments, thus forming a small angle [37,38]. This leads to the generation of weak ferromagnetic characteristics in antiferromagnetic YFeO_3 ceramics and increases with the refinement of grain size. Because the grains of the 1000 °C-sintered sample are smaller than those of the 1050 °C-sintered one, the magnetic properties of the 1000 °C-sintered sample, such as M_m (maximum magnetization) and M_r (remnant magnetization), are higher. Both the 1000 °C and 1050 °C-sintered samples exhibit anti-ferromagnetic characteristics. The M_m , M_r , and H_c (coercive field) are about 3.00 emu/g, 0.91 emu/g, and 790 Oe, respectively, for the 1000 °C-sintered sample, while these are about 2.16 emu/g, 0.86 emu/g, and 6150 Oe for the 1050 °C-sintered sample. The H_c value of the 1000 °C-sintered sample is smaller while its M_m and M_r values are larger compared to the 1050 °C-sintered sample. In order to make a comparison, some relevant magnetic parameters of YFeO_3

are presented in Table 1 [9–11,14,38,39]. Obviously, the M_m value of the 1000 °C-sintered sample is much larger than that in the reported data. Moreover, the coercive field (H_c) is the same order of magnitude as that of the YFeO_3 sample prepared by Ma et al. [10]. Compared with the results of Ma et al. and other reports [10,40], the present values of M_r and M_m are much higher than those of the samples fabricated by a conventional sintering method because of the smaller grain size and less impurity.

Table 1. Comparison of the relevant magnetic parameters for YFeO_3 ceramics.

No.	M_m (emu/g)	H_c (kOe)	Reference
1	1.9@7.0 T	24.6	[9]
2	0.46@0.65 T	0.25	[11]
3	0.15@0.25 T	0.97	[38]
4	0.45@0.35 T	0.25	[14]
5	2.1@5 T	1.0	[10]
6	3.0@6 T	0.91	Present work

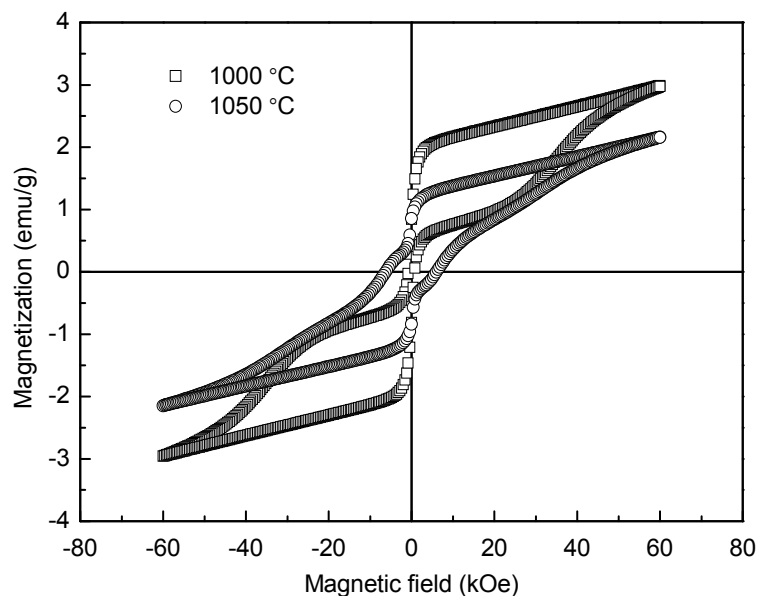


Figure 9. Magnetic hysteresis loops of the YFeO_3 ceramic samples sintered at 1000 °C and 1050 °C.

4. Conclusions

Briefly summarizing the work performed and the results obtained, the high-density impurity-free YFeO_3 ceramics with grain sizes in the 1–2 μm range were prepared by combining a low-temperature solid reaction and spark plasma sintering at 1000 °C, along with annealing in air at 800 °C for 2 h. However, the samples sintered at 900, 950, and 1050 °C were found to possess a lower density and small amounts of impurity. The relative density of the 1000 °C-sintered sample was as high as 97% while that of the 1050 °C-sintered sample was just about 95%. The XPS showed that the Fe^{3+} ions took up the majority of Fe ions with a low concentration of Fe^{2+} ions while the 1050 °C-sintered sample experienced an increase in the concentration of oxygen vacancies during the fabrication procedure. Finally, the dielectric behavior was impacted by the sintering temperature. The dielectric constant of the 1000 °C-sintered sample was found to be much higher than that of the 1050 °C-sintered sample. The higher M_m and M_r values of the 1000 °C-sintered sample were attributed to the refined grain size and high purity composition. In summary, one can conclude that the YFeO_3 ceramics prepared by combining low-temperature solid reaction and spark plasma sintering as described in this report have excellent dielectric and magnetic properties.

Acknowledgments: This work was supported by the International S&T Cooperation Program of China (2014DFA53020), Guangdong Innovative and Entrepreneurial Research Team Program (No. 2013C099), Science and Technology Foundation of Shenzhen under Grant No. JCYJ20140417172417172.

Author Contributions: Meng Wang, Ting Wang, and Shenhua Song conceived and designed the experiments; Meng Wang performed the experiments; Meng Wang and Ting Wang analyzed the data; Qing Ma and Renchen Liu contributed analysis tools; Meng Wang wrote the paper.

Conflicts of Interest: The authors declare no conflict of interest.

References

1. Dho, J.; Blamire, M. Competing functionality in multiferroic YMnO₃. *Appl. Phys. Lett.* **2005**, *87*, 252504. [[CrossRef](#)]
2. Wang, L.J.; Feng, S.M.; Zhu, J.L.; Yu, R.C.; Jin, C.Q.; Yu, W.; Wang, X.H.; Li, L.T. Ferroelectricity of multiferroic hexagonal TmMnO₃ ceramics synthesized under high pressure. *Appl. Phys. Lett.* **2007**, *91*, 172502. [[CrossRef](#)]
3. Hemberger, J.; Schrettle, F.; Pimenov, A.; Lunkenheimer, P.; Ivanov, V.Y.; Mukhin, A.A.; Balbashov, A.M.; Loidl, A. Multiferroic phases of Eu_{1-x}Y_xMnO₃. *Phys. Rev. B Condens. Matter* **2007**, *75*, 5118. [[CrossRef](#)]
4. Katsufuji, T.; Mori, S.; Masaki, M.; Moritomo, Y.; Yamamoto, N.; Takagi, H. Dielectric and magnetic anomalies and spin frustration in hexagonal RMnO₃ (R = Y, Yb, and Lu). *Phys. Rev. B Condens. Matter* **2001**, *64*, 115–149. [[CrossRef](#)]
5. Traversa, E.; Nunziante, P.; Sangaletti, L.; Allieri, B.; Depero, L.E.; Aono, H.; Sadaoka, Y. Synthesis and structural characterization of trimetallic perovskite-type rare-earth orthoferrites, La_xSm_{1-x}FeO₃. *J. Am. Ceram. Soc.* **2000**, *83*, 1087–1092. [[CrossRef](#)]
6. Cherry, M.; Islam, M.S.; Catlow, C.R.A. Oxygen ion migration in perovskite-type oxides. *J. Solid State Chem.* **1995**, *118*, 125–132. [[CrossRef](#)]
7. Minh, N.Q. Ceramic fuel cells. *J. Am. Ceram. Soc.* **1993**, *76*, 563–588. [[CrossRef](#)]
8. Sharon, M.; Prasad, B.M. Preparation and photocharacterization of YFeO₃ semiconductor. *Electrochim. Acta* **1985**, *30*, 331–334. [[CrossRef](#)]
9. Mathur, S.; Veith, M.; Rapalaviciute, R.; Shen, H.; Goya, G.F.; Filho, W.L.M.; Berquo, T.S. Molecule derived synthesis of nanocrystalline YFeO₃ and investigations on its weak ferromagnetic behavior. *Chem. Mater.* **2004**, *16*, 1906–1913. [[CrossRef](#)]
10. Ma, Y.; Chen, X.M.; Lin, Y.Q. Relaxorlike dielectric behavior and weak ferromagnetism in YFeO₃ ceramics. *J. Appl. Phys.* **2008**, *103*, 124111. [[CrossRef](#)]
11. Wu, L.; Yu, J.C.; Zhang, L.; Wang, X.; Li, S. Selective self-propagating combustion synthesis of hexagonal and orthorhombic nanocrystalline yttrium iron oxide. *J. Solid State Chem.* **2004**, *177*, 3666–3674. [[CrossRef](#)]
12. Racu, A.V.; Ursu, D.H.; Kuliukova, O.V.; Logofatu, C.; Leca, A.; Miclau, M. Direct low temperature hydrothermal synthesis of YFeO₃ microcrystals. *Mater. Lett.* **2015**, *140*, 107–110. [[CrossRef](#)]
13. Shang, M.; Wang, C.; Chen, Y.; Sun, F.; Yuan, H. The multiferroic epitaxial thin film YFeO₃. *Mater. Lett.* **2016**, *175*, 23–26. [[CrossRef](#)]
14. Zhang, W.; Fang, C.; Yin, W.; Zeng, Y. One-step synthesis of yttrium orthoferrite nanocrystals via sol-gel auto-combustion and their structural and magnetic characteristics. *Mater. Chem. Phys.* **2013**, *137*, 877–883. [[CrossRef](#)]
15. Rearick, T.M. Combined magnetic-dipole and electric-quadrupole hyperfine interactions in rare-earth orthoferrite ceramics. *Phys. Rev. B Condens. Matter* **1993**, *48*, 224–238. [[CrossRef](#)] [[PubMed](#)]
16. Eibschütz, M.; Shtrikman, S.; Treves, D. Mössbauer studies of Fe₅₇ in orthoferrites. *Phys. Rev.* **1967**, *156*, 562–577. [[CrossRef](#)]
17. Li, F.; Wang, H.; Wang, L.; Wang, J. Magnetic properties of ZnFe₂O₄ nanoparticles produced by a low-temperature solid-state reaction method. *J. Magn. Magn. Mater.* **2007**, *309*, 295–299. [[CrossRef](#)]
18. Wang, X.; Padture, N.P.; Tanaka, H. Contact-damage-resistant ceramic/single-wall carbon nanotubes and ceramic/graphite composites. *Nat. Mater.* **2004**, *3*, 539–544. [[CrossRef](#)] [[PubMed](#)]
19. Isobe, T.; Daimon, K.; Sato, T.; Matsubara, T.; Hikichi, Y.; Ota, T. Spark plasma sintering technique for reaction sintering of Al₂O₃/Ni nanocomposite and its mechanical properties. *Ceram. Int.* **2008**, *34*, 213–217. [[CrossRef](#)]

20. Zhang, Y.; Zhang, J.; Lu, Q. Synthesis of highly textured $\text{Ca}_3\text{Co}_4\text{O}_9$ ceramics by spark plasma sintering. *Ceram. Int.* **2007**, *33*, 1305–1308. [[CrossRef](#)]
21. Shimojo, Y.; Wang, R.; Shan, Y.J.; Izui, H.; Taya, M. Dielectric characters of $0.7\text{Pb}(\text{Mg}_{1/3}\text{Nb}_{2/3})\text{O}_3-0.3\text{PbTiO}_3$ ceramics fabricated at ultra-low temperature by the spark-plasma-sintering method. *Ceram. Int.* **2008**, *34*, 1449–1452. [[CrossRef](#)]
22. Ma, Y.; Wu, Y.J.; Chen, X.M.; Cheng, J.P.; Lin, Y.Q. In situ synthesis of multiferroic YMnO_3 ceramics by SPS and their characterization. *Ceram. Int.* **2009**, *35*, 3051–3055. [[CrossRef](#)]
23. Ma, Y.; Wu, Y.J.; Lin, Y.Q.; Chen, X.M. Microstructures and multiferroic properties of $\text{YFe}_{1-x}\text{Mn}_x\text{O}_3$ ceramics prepared by spark plasma sintering. *J. Mater. Sci. Mater. Electron.* **2010**, *21*, 838–843. [[CrossRef](#)]
24. Song, S.H.; Zhu, Q.S.; Weng, L.Q.; Mudinepalli, V.R. A comparative study of dielectric, ferroelectric and magnetic properties of BiFeO_3 multiferroic ceramics synthesized by conventional and spark plasma sintering techniques. *J. Eur. Ceram. Soc.* **2015**, *35*, 131–138. [[CrossRef](#)]
25. Wang, T.; Song, S.H.; Wang, M.; Li, J.Q.; Ravi, M. Effect of annealing atmosphere on the structural and electrical properties of BiFeO_3 multiferroic ceramics prepared by sol-gel and spark plasma sintering techniques. *Ceram. Int.* **2016**, *42*, 7328–7335. [[CrossRef](#)]
26. Mudinepalli, V.R.; Song, S.; Li, J.; Murty, B.S. Effect of grain size on the electrical properties of high dense BPT nanocrystalline ferroelectric ceramics. *Ceram. Int.* **2014**, *40*, 1781–1788. [[CrossRef](#)]
27. Gao, Y.; Wu, Y.J.; Xiang, M.C.; Cheng, J.P.; Lin, Y.Q.; Ma, Y. Dense YMn_2O_5 ceramics prepared by spark plasma sintering. *J. Am. Ceram. Soc.* **2008**, *91*, 3728–3730. [[CrossRef](#)]
28. Schmool, D.S.; Keller, N.; Guyot, M.; Krishnan, R.; Tessier, M. Magnetic and magneto-optic properties of orthoferrite thin films grown by pulsed-laser deposition. *J. Appl. Phys.* **1999**, *86*, 5712–5717. [[CrossRef](#)]
29. Muneeswaran, M.; Dhanalakshmi, R.; Giridharan, N.V. Structural, vibrational, electrical and magnetic properties of $\text{Bi}_{1-x}\text{Pr}_x\text{FeO}_3$. *Ceram. Int.* **2015**, *41*, 8511–8519. [[CrossRef](#)]
30. Moulder, J.F.; Stickle, W.F.; Sobol, P.E.; Bomben, K.D.; Chastain, J.; King, R.C. *Handbook of X-ray Photoelectron Spectroscopy*; Perkin-Elmer Corporation: Eden Prairie, MN, USA, 1992.
31. Aono, H.; Sato, M.; Traversa, E.; Sakamoto, M.; Sadaoka, Y. Design of ceramic materials for chemical sensors: Effect of SmFeO_3 processing on surface and electrical properties. *J. Am. Ceram. Soc.* **2001**, *84*, 341–347. [[CrossRef](#)]
32. Vaqueiro, P.; Lópezquintela, M.A. Influence of complexing agents and pH on Yttrium-Iron garnet synthesized by the sol-gel method. *Chem. Mater.* **1997**, *9*, 2836–2841. [[CrossRef](#)]
33. Elissalde, C.; Ravez, J. Ferroelectric ceramics: Defects and dielectric relaxation. *J. Mater. Chem.* **2001**, *11*, 1957–1967. [[CrossRef](#)]
34. Ray, G.; Sinha, N.; Kumar, B. Environment friendly novel piezoelectric $0.94[\text{Na}_{0.8}\text{K}_{0.2}\text{NbO}_3]-0.06\text{LiNbO}_3$ ternary ceramic for high temperature dielectric and ferroelectric applications. *Mater. Chem. Phys.* **2013**, *142*, 619–625. [[CrossRef](#)]
35. Wang, S.-F.; Dayton, G.O. Dielectric properties of fine-grained barium titanate based X7R materials. *J. Am. Ceram. Soc.* **1999**, *82*, 2677–2682. [[CrossRef](#)]
36. Arlt, G.; Hennings, D.; With, G.D. Dielectric properties of fine-grained barium titanate ceramics. *J. Appl. Phys.* **1985**, *58*, 1619–1625. [[CrossRef](#)]
37. Moriya, T. New mechanism of anisotropic superexchange interaction. *Phys. Rev. Lett.* **1960**, *4*, 228–230. [[CrossRef](#)]
38. Dzyaloshinsky, I. A thermodynamic theory of weak ferromagnetism of antiferromagnetics. *J. Phys. Chem. Solids* **1958**, *4*, 241–255. [[CrossRef](#)]
39. Shen, H.; Xu, J.; Wu, A.; Zhao, J.; Shi, M. Magnetic and thermal properties of perovskite YFeO_3 single crystals. *Mater. Sci. Eng. B* **2009**, *157*, 77–80. [[CrossRef](#)]
40. Yuan, X.; Sun, Y.; Xu, M. Effect of Gd substitution on the structure and magnetic properties of YFeO_3 ceramics. *J. Solid State Chem.* **2012**, *196*, 362–366. [[CrossRef](#)]

